Aalborg University

DENMARK

Maximum Virtual Inertia From DC-Link Capacitors Considering System Stability at Voltage Control Timescale

Peng, Qiao; Fang, Jingyang; Yang, Yongheng; Liu, Tianqi; Blaabjerg, Frede

Maximum Virtual Inertia from DC-Link Capacitors Considering System Stability at Voltage Control Timescale

Qiao Peng, *Member, IEEE,* Jingyang Fang, *Member, IEEE,* Yongheng Yang, *Senior Member, IEEE,*
Tianqi Liu, *Senior Member, IEEE,* and Frede Blaabjerg, *Fellow, IEEE*

Abstract—In power electronics-dominant systems (PEDSs), the declining-inertia issue is one of the most significant challenges to tackle. The inertia emulation from DC-link capacitors is one cost-effective and application-friendly solution to enhance the system inertia. Although the virtual inertia control of the DC-link capacitor supports the grid frequency with a relatively long-term effect, it affects the dynamic of the power converter at multiple timescales. In turn, the maximum effective virtual inertia from the DC-link capacitor is limited by the operation condition of the converter. Thus, to properly design the virtual inertia control, the dynamics of the faster timescale than the inertia emulation should be addressed. With the above, this paper analyzes the maximum virtual inertia of DC-link capacitors based on a multi-timescale model of power converters. First, the system stability considering virtual inertia control of DC-link capacitors is analyzed in the submodel at the voltage control timescale (VCT), where the virtual inertia control parameters are accordingly tuned on a pre-designed converter. Then, the maximum effective virtual inertia is identified in the submodel at the rotor motion timescale (RMT). The exploration and findings in this paper are beneficial to the power converter design and future inertia placement optimization in PEDSs. Case studies on a hardware-in-the-loop platform are conducted to validate the proposed model and the analysis method.

Index Terms—Power electronic converters, capacitors, virtual inertia, frequency control, multi-timescale, power-internal voltage model

I. INTRODUCTION

THE modern power grid is being penetrated by miscellaneous distributed energy resources (DER), which are generally integrated to the grid through power electronic converters. Consequently, the power electronics-dominant systems (PEDS) emerge, which will lay the foundation of future power grid, and it is also driven by the development of power electronics technologies [1]. However, the power electronics

Q. Peng is with the College of Electrical Engineering, Sichuan University, Chengdu 610065, China and the Department of Energy Technology, Aalborg University, Aalborg 9220, Denmark (e-mail: qpeng@scu.edu.cn).

J. Fang is with the Department of Electrical and Computer Engineering, Duke University, Durham, NC 27710, USA (e-mail: jingyang.fang@duke.edu).

Y. Yang is with the College of Electrical Engineering, Zhejiang University, Hangzhou 310027, China (e-mail: yh.yang@ieee.org).

T. Liu is with the College of Electrical Engineering, Sichuan University, Chengdu 610065, China (e-mail: tqliu@scu.edu.cn).

F. Blaabjerg is with the Department of Energy Technology, Aalborg University, Aalborg 9220, Denmark (e-mail: fbl@et.aau.dk).

also introduce several stability issues to the power systems, one of which is the weakness in response to frequency incidents. Without specially designed measures, the DERs would rarely support the grid frequency, and even in worse cases, they may trip from the main grid under severe frequency incidents. This has been experienced by the power grids in South Australia and the UK, where similar extreme weather resulted in frequency collapses and further blackouts [2], [3]. The possible reasons for these frequency incidents may include the imperfect fault ride-through abilities of the DERs and the inertia decrease in the PEDSs.

The inertia in conventional synchronous generators (SG)-based power systems is physically generated by rotors of huge rotating mass. When the SGs are replaced by DERs, the physical inertia decreases, and the systems may lose the capability to resist severe disturbances, especially frequency incidents [4]. Thus, the utility imposes stringent requirements for the DERs to provide ancillary frequency support, including alternative inertia to the grid [5]–[7]. For instance, according to the IEEE standard for interconnection and interoperability of DERs connected to main grid [6], the DERs shall have the capability of mandatory operation with frequency-droop during abnormal conditions, while the inertia response of DERs is greatly encouraged.

In general, there are two popular solutions for alternative inertia provision of DERs and power converters. The first one is to emulate inertia from grid-feeding converters by directly regulating the power transferred from renewable energy, e.g., from wind turbines and photovoltaic (PV) panels. To achieve so, the DERs should reserve an amount of power to flexibly deal with over-frequency and under-frequency issues [8], [9]. The de-rating operation limits the optimal power production of DERs, which is not always desired. Furthermore, in grid-feeding converters, the accurate measurement of the rate of change of frequency (RoCoF) for inertia emulation is an intractable challenge [10], [11].

Another popular solution is to provide virtual inertia from energy storage systems (ESS). This solution is usually implemented in grid-forming converters [12]. More specifically, grid-forming converters with second-order active power-frequency droop characteristics [13], e.g., the traditional droop control with a low-pass filter [14], the virtual synchronous generator (VSG) [15], and the virtual synchronous machine (VSM) [16] are designed to emulate SGs and generate virtual inertia from power converters. Nevertheless, the virtual inertia is usually supported by large-capacity ESSs (e.g., batteries or supercapacitors) connected to the power converters, which

makes the application limited by economic consideration. Notably, although the grid-forming converters can be also supported by DC-link capacitors [17], [18], it, however, may be relatively weak to form the grid. Additionally, it is not efficient to assign more grid-forming converters with inertia emulation in the grid, as the power converters would be unable to respond immediately in some cases, e.g., when the transmission power is reset by the system operator. In such a case, the superiority of power electronics, i.e., flexible control and fast response, is submerged.

For more general applications, the virtual inertia emulated by the plug-in DC-link voltage control loop in grid-feeding converters emerged [19]–[22], which is achieved by employing a DC-link voltage control loop into the basic control of the grid-feeding converters. The advantages of this inertia emulation strategy can be summarized as follows:

- Real-time RoCoF measurement is not required, as the second-order droop characteristic can be realized by the natural charging/discharging of DC-link capacitors.
- Basic control system of power converters is not altered, while the inertia emulation can be activated when needed.
- No extra equipment, e.g., large-scale ESSs, is required. That is, the overall cost is maintained.

Furthermore, as the DC-link capacitor is one of the fundamental components in the power converters, the numerous DC-link capacitors in the PEDSs can effectively contribute to the inertia enhancement, especially in the emergency circumstances. Thus, the inertia emulation of DC-link capacitors is worthy for development. However, the systematic method to identify the maximum virtual inertia that the DC-link capacitors can provide with stability consideration has been barely reported.

For instance, in [19]–[22], the design of the virtual inertia from the DC-link capacitors mainly considered the rated frequency, DC-link voltage level, and converter capacity, etc., where the impact of the inertia emulation on the stability of converter and grid was ignored. When introducing the inertia emulation of DC-link capacitors into the basic control system, it inevitably affects the stability of the power converters, and it may make the system out of the stable region in certain cases. Thus, the stability margin of the pre-designed power converters limits the inertia provision of the DC-link capacitors, which should be considered when tuning the inertia emulation control. Additionally, the quantitative identification of virtual inertia is also a challenge. From the perspective of the grid, the accurate inertia identification helps the frequency stability estimation and further the future inertia placement and optimization. Thus, the effective virtual inertia that can profitably support the grid frequency should be accurately identified, which is also ignored in the literature.

To analyze the impact of the inertia emulation on the system stability as well as the effective inertia identification, the multi-timescale analysis is required, as the system dynamics at different timescales should be addressed. The timescale-focused analysis method presented in [23], [24] can be adopted. For different objectives, the models at different timescales can be developed. As for the inertia analysis, various models of power converters focusing on different timescales were proposed. For instance, an SG-mimicking model of a wind turbine at the rotor motion timescale (RMT) was proposed in [25] to assess the transient stability. The models in analogy with the SG were developed in [26], [27] to analyze the stability at the voltage control timescale (VCT). It was also applied in [28] to discuss the stability of modular multilevel converters at the VCT. Moreover, a similar concept can be found in [29] to address the transient stability of power converters at the VCT. However, all those models have not been applied to assess the virtual inertia control of the DC-link capacitors. More importantly, those models focusing on a single timescale, which is not sufficient for the maximum virtual inertia identification. In this context, a multi-timescale model is demanded.

In light of the above, this paper explores the maximum virtual inertia from DC-link capacitors. The main contributions are summarized as follows:

1) A multi-timescale power-internal voltage (PIV) model of power converters is proposed. It consists of interrelated submodels, which can reflect the system dynamics at different timescales.
2) The PIV model is open-loop, which is independent of grid parameters. Then, the closed-loop system model can be obtained by aggregating power converter models to the grid model. In this way, the analysis of systems consisting of multiple converters becomes more convenient.
3) The impact of inertia emulation on system stability at the VCT is addressed, based on which the virtual inertia control of DC-link capacitors is properly tuned. The resultant virtual inertia control can be an effective and universal solution for the PEDSs.
4) The effective virtual inertia that can profitably support the grid frequency is identified. It makes the inertia placement and optimization at the system level become possible.

The rest of the paper is organized as follows. In Section II, the virtual inertia control of the DC-link capacitor is introduced. The multi-timescale PIV model for power converters is demonstrated in Section III, and the maximum virtual inertia is identified in Section IV. In Section V, the proposed model and method are verified through a case study on a hardware-in-loop system. Finally, concluding remarks are provided in Section VI.

II. Virtual Inertia Control of DC-Link Capacitors

In the conventional AC grid, the frequency is regulated by the SG rotors. Specifically, the frequency is determined by the rotational velocity of the rotor, which is affected by the power balance of the rotor, i.e., the difference between the input mechanical power and the output electromagnetic power. When the power balance is disturbed, the rotor motion state (i.e., the rotation) will be altered, which will further change the frequency. However, the mechanical inertia of the rotor will resist the motion change, which makes the rotor gradually move to a new motion state, instead of a sudden change. In such a case, the frequency will also gradually change to a new state. Due to this inherent feature of SG rotors, the operation and control rules of the conventional power systems are generally established according to the inertia characteristics [30]. Thus, when the conventional SGs are
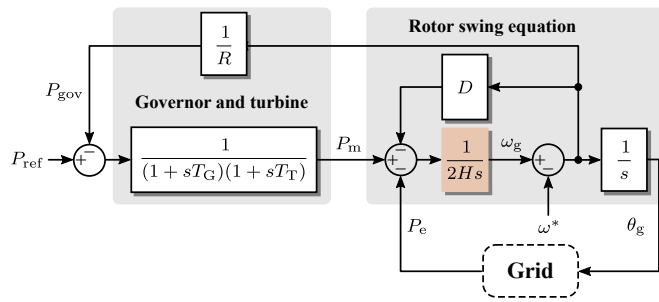
Fig. 1. Control diagram of an SG, where P_{ref} and P_{gov} represent the SG active power reference and the additional active power reference from the governor, T_{G} and T_{T} are the governor and turbine time constants, and R is the frequency-power droop coefficient.

replaced by the DERs with power converters, the alternative inertia should be provided in case of frequency collapse.

When the grid frequency is governed by the SG, the swing equation, i.e., the rotor motion equation, is given as [31]

$$\begin{cases} P_{\text{m}} - P_{\text{e}} = 2H\dfrac{d\omega_{\text{g}}}{dt} + D(\omega_{\text{g}} - \omega^*) \\ \dfrac{d\theta_{\text{g}}}{dt} = \omega_{\text{g}} - \omega^* \end{cases}, \qquad (1)$$

in which P_{m} and P_{e} are the mechanical power input to the rotor and the electromagnetic power output to the grid, respectively, H and D are the inertia constant and the damping coefficient, ω_{g} and ω^* are the angular frequency of the SG and the nominal angular frequency, and θ_{g} is the internal voltage phase angle of the SG.

The control diagram including the swing equation of the SG is further shown in Fig. 1. It can be seen in (1) and Fig. 1 that there are two loops between the power and the frequency in the swing equation, i.e., the inertia loop and the damping loop. In the inertia loop, the power and frequency are in the second-order droop relationship, of which the gain is determined by the inertia constant. That is to say, for a power generating unit with virtual inertia provision, its output power should be regulated in proportion to the differential of the frequency, i.e., the RoCoF.

Inspired by this, the DC-link capacitors in power converters can be adopted for virtual inertia provision, as the power and DC-link voltage are also in the second-order droop relationship due to the charging/discharging characteristic of the capacitor. Specifically, the relationship between the DC-link voltage and the active power bridged by the DC-link capacitor is given as

$$P_{\text{in}} - P = C_{\text{dc}} v_{\text{dc}} \frac{dv_{\text{dc}}}{dt}, \qquad (2)$$

where v_{dc} is the DC-link voltage, C_{dc} is the DC-link capacitance, P_{in} is the active power input from the DC side, and P is the power injected to the converter after the DC-link capacitor. When ignoring the power loss of converters, P can be considered to be the converter output power.

It can be seen in (2) that the DC-link voltage and the power have the second-order droop characteristic. To generate virtual inertia, the DC-link voltage should be controlled in proportion to the frequency. Then, the second-order power-frequency relationship can be established for the DC-link capacitor, and

the inertia can be emulated. To achieve so, the DC-link voltage should be regulated by

$$v_{\text{dc}}^f = k_{\omega v}\omega, \qquad (3)$$

in which ω is the grid angular frequency, v_{dc}^f is the DC-link voltage reference deviation introduced by the frequency-voltage droop loop, and $k_{\omega v}$ is the droop coefficient.

With the virtual inertia control shown in (3), the DC-link voltage reference considering the inertia emulation becomes

$$v_{\text{dc}}^r = v_{\text{dc}}^* + v_{\text{dc}}^f, \qquad (4)$$

with v_{dc}^* being the rated DC-link voltage. When focusing on the RMT, the dynamics at faster timescales, including the DC-link voltage control loop, can be ignored (the modeling at different timescales will be demonstrated later). Consequently, the DC-link voltage can immediately follow the reference, i.e.,

$$v_{\text{dc}} = v_{\text{dc}}^r. \qquad (5)$$

Substituting (3)–(5) into (2) yields

$$P_{\text{in}} - P = C_{\text{dc}}(v_{\text{dc}}^* + v_{\text{dc}}^f)k_{\omega v}\frac{d\omega}{dt}. \qquad (6)$$

As v_{dc}^f is limited by the allowed DC-link voltage deviation, it is relatively small compared with v_{dc}^*, which can be ignored in (6). Then, the virtual inertia provided by the DC-link capacitor is identified by comparing (6) with (1) as

$$H_v = \frac{1}{2}C_{\text{dc}}v_{\text{dc}}^* k_{\omega v}, \qquad (7)$$

which implies that the virtual inertia is determined by the DC-link capacitance, the rated DC-link voltage, and the frequency-voltage droop gain. Notably, the virtual inertia control of DC-link capacitors is an addition to the basic DC-link voltage control. Thus, the basic control parameters are pre-designed. That is to say, the DC-link capacitor and the rated DC-link voltage are settled in (7). Then, the virtual inertia that the DC-link capacitor can provide is determined by the frequency-voltage droop coefficient, $k_{\omega v}$. In turn, the maximum virtual inertia identification is essential to design the proper $k_{\omega v}$ under certain operation conditions, as the focus of this paper.

To properly design $k_{\omega v}$, not only the dynamic at the RMT, but also the dynamics at faster timescales should be considered. Otherwise, the designed droop coefficient $k_{\omega v}$ may lead to instability. More specifically, the grid frequency in (3) is usually obtained by a particular control loop, e.g., the phase-locked loop (PLL), of which the dynamic should be considered. Furthermore, (5) is tenable based on the assumption that the DC-link voltage controller can follow the reference immediately, which should be reconsidered in the stability analysis. Thus, in order to properly design $k_{\omega v}$ and identify the maximum effective virtual inertia, a multi-timescale model and a corresponding analysis method of power converters are needed.
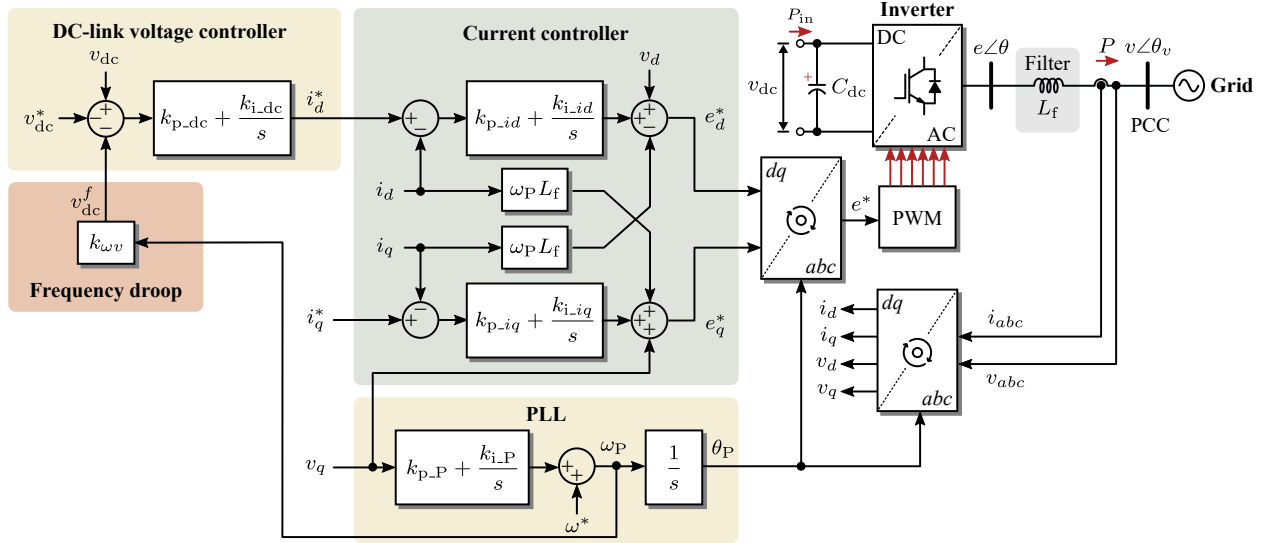
Fig. 2. Dual-loop current control diagram of the grid-connected power converters with frequency-voltage droop control loop, where e and v are the amplitudes of the internal voltage and terminal voltage, respectively, with θ and θ_v being their phase angles, the superscript "*" indicates the corresponding reference or the rated value and the subscripts "d", "q" denote the d-axis and q-axis component, respectively (PWM – pulse width modulation; PLL – phase-locked loop).

TABLE I
APPLICATION OF THE SUBMODELS AT DIFFERENT TIMESCALES.

Submodel	Timescale	Potential application
At the RMT	Large	• Inertia emulation control analysis • DC-link capacitor charging analysis
At the VCT	Medium	• DC-link voltage stability analysis • Frequency control stability analysis
At the CCT	Small	• Harmonics resonance analysis • Weak grid-connected stability analysis

III. SMALL-SIGNAL MULTI-TIMESCALE PIV MODEL OF POWER CONVERTERS

The multi-timescale model should have several submodels to facilitate different functionalities. Before the modeling, the following should be clarified:

- *Timescale selection*: For various objectives, one or more submodels can be considered, while the others are discarded. With this concept, the potential applications of the submodels for different focuses are summarized in Table I, where CCT stands for the current control timescale. As aforementioned, the virtual inertia supports the grid frequency at the RMT as the mechanical inertia of the SG rotor does. On the other hand, the frequency for the virtual inertia emulation comes from the PLL, and the DC-link capacitor dynamics are highly affected by the voltage controller. Thus, the focus of this paper will be on the RMT and VCT according to Table I. Notably, in certain special cases, the dynamic of the pre-designed current control loop is not much faster than the voltage control loop. Then, the timescale-focused modeling method should be carefully utilized due to potential interaction between different timescales [32].
- *Submodel interconnection*: The connection between sub-models is important. For the submodels at faster

timescales, they can be simplified to the submodels at slower timescales. For example, the modules containing proportional-integral (PI) controllers can be ignored by assuming that they respond sufficiently fast to track the references, i.e., the input variables become zero.

- *Identical external characteristic*: The submodels should have the same input and output states, based on which the focused features can remain when simplifying the submodel to a slower timescale. As shown in Fig. 1, the inertia constant and the damping coefficient determine the relationship between active power, frequency, and internal voltage. That is, the inertia dynamic of an SG can be reflected by the PIV characteristic. Thus, the multi-timescale model proposed in this paper will represent the PIV characteristics of power converters.
- *Basic control strategy*: The dual-loop current control is adopted in this paper as the basic control strategy, where the DC-link voltage control is the foundation of inertia emulation. The control system with the additional frequency-voltage droop loop for inertia emulation is shown in Fig. 2, of which the rest parameters will be defined in the modeling. The power converters with different basic control strategies can also be modeled similarly, based on which the multi-timescale PIV char-acteristics of converters can be revealed.

For simplicity, the resistances of the line and the filter in the system shown in Fig. 2 are neglected. The resistance mainly affects the system dynamics at the CCT [26], which is out of the scope of this paper.

A. DC-Link Capacitor Dynamic

If P_{in} is constant in (2), it can be linearized around the equilibrium state as

$$\frac{d\Delta v_{\text{dc}}}{dt} = k_{Pv}\Delta P, \qquad (8)$$

with

$$k_{Pv} = -\frac{1}{C_{\mathrm{dc}}v_{\mathrm{dc0}}}, \tag{9}$$

where the subscript "0" indicates the equilibrium value (i.e., the steady-state value if the small-signal stability around the steady-state is addressed) and the prefix "Δ" indicates the small-signal perturbation from the equilibrium value. The linearized model of the frequency-droop loop can then be obtained from (3) as

$$\Delta v_{\mathrm{dc}}^{f} = k_{\omega v}\Delta\omega_{\mathrm{P}}. \tag{10}$$

B. DC-Link Voltage Controller

The DC-link voltage control will generate the reference of the d-axis current controller, as shown in Fig. 2. Considering a PI controller, the linearized model of the DC-link voltage controller is then given as

$$\Delta i_d^* = k_{\mathrm{p\_dc}}(\Delta v_{\mathrm{dc}} - \Delta v_{\mathrm{dc}}^* - \Delta v_{\mathrm{dc}}^{\mathrm{f}}) + k_{\mathrm{i\_dc}}\Delta\varphi_{\mathrm{dc}}, \tag{11}$$

where i_d is the d-axis current, $k_{\mathrm{p\_dc}}$ and $k_{\mathrm{i\_dc}}$ are the proportional and integral coefficients for the DC-link voltage PI controller, respectively, the superscript "$*$" denotes the reference value, and $\Delta\varphi_{\mathrm{dc}}$ is defined as

$$\frac{d\Delta\varphi_{\mathrm{dc}}}{dt} = \Delta v_{\mathrm{dc}} - \Delta v_{\mathrm{dc}}^* - \Delta v_{\mathrm{dc}}^{\mathrm{f}}. \tag{12}$$

As for the q-axis current controller, it is generally designed for specific requirements of the reactive power. In this paper, the focus is on the dynamics of active power, DC-link voltage, and frequency. Thus, the reactive power regulation is ignored, and the reference of the q-axis current i_q is given as

$$i_q^* = 0. \tag{13}$$

C. Phase-Locked Loop

The PLL is in charge of the grid synchronization of power converters, based on which the synchronous rotating reference frame (dq-frame) is established. Although the exploration on the PLL-independent strategy is vigorous, the PLL, especially the synchronous reference frame PLL (SRF-PLL), is still the most popular solution for grid synchronization. Thus, the SRF-PLL is adopted in this paper, and the configuration of the SRF-PLL is also shown in Fig. 2.

The voltage relationship in the dq-frame formed by the PLL is shown in Fig. 3, where the parameters in the steady-state and after being disturbed are presented. In Fig. 3, $\boldsymbol{E}$ and $\boldsymbol{V}$ are the vectors of the internal voltage and the terminal voltage, θ_{P} is the terminal voltage phase angle detected by the PLL, θ_e^{P} is the phase angle difference between the internal voltage and the d-axis ($\theta_e^{\mathrm{P}} = \theta - \theta_{\mathrm{P}}$), and θ_v^{P} is the phase angle difference between the terminal voltage and the d-axis ($\theta_v^{\mathrm{P}} = \theta_v - \theta_{\mathrm{P}}$). It can be seen in Fig. 3 that in the steady-state, the PLL can track the grid voltage phase angle accurately, i.e., $\theta_{v0}^{\mathrm{P}} = 0$, and the d-axis conforms with the terminal voltage vector $\boldsymbol{V}$. However, when the system is disturbed, the PLL is unable to follow the system dynamic immediately, and then, there will be a deviation between $\boldsymbol{V}$ and the d-axis, resulting in $\Delta\theta_v^{\mathrm{P}}$. It will affect the entire control system and further system stability.

Fig. 3. Voltage relationship in the dq-frame formed by the PLL in the steady-state and when being disturbed, where the superscript "$\prime$" denotes the values after disturbance.

The control equation of the SRF-PLL in the complex frequency domain is given as

$$\theta_{\mathrm{P}} = [v_q(k_{\mathrm{p\_P}} + \frac{k_{\mathrm{i\_P}}}{s}) + \omega^*]\frac{1}{s}, \tag{14}$$

where $k_{\mathrm{p\_P}}$ and $k_{\mathrm{i\_P}}$ are the proportional and integral coefficients of the PI controller (i.e., the loop filter) for the PLL, respectively. Linearizing (14) yields

$$\Delta\theta_{\mathrm{P}} = v_0\Delta\theta_v^{\mathrm{P}}(k_{\mathrm{p\_P}} + \frac{k_{\mathrm{i\_P}}}{s})\frac{1}{s}. \tag{15}$$

Considering that the terminal voltage amplitude is close to the rated value in the steady-state, i.e., $v_0 \approx 1$, the linearized model of the SRF-PLL in the time domain can be obtained as

$$\frac{d\Delta\theta_{\mathrm{P}}}{dt} = k_{\mathrm{p\_P}}\Delta\theta_v^{\mathrm{P}} + k_{\mathrm{i\_P}}\Delta\varphi_{\mathrm{P}}, \tag{16}$$

with $\Delta\varphi_{\mathrm{P}}$ being defined as

$$\frac{d\Delta\varphi_{\mathrm{P}}}{dt} = \Delta\theta_v^{\mathrm{P}}. \tag{17}$$

D. Filter Dynamic

The filter dynamic is important in the power converter modeling, as it provides information about the voltage and active power relationship between the internal voltage and the terminal voltage, see Fig. 2. By properly modeling the filter, the open-loop model of the power converter can be obtained without the grid parameters, which benefits its application in multiple converter-based systems.

The voltage drop on the filter is given as

$$\boldsymbol{E} = \boldsymbol{V} + jX_{\mathrm{f}}\boldsymbol{I}, \tag{18}$$

where $\boldsymbol{I}$ is the converter output current vector and X_{f} is the inductive reactance corresponding to the filter inductor L_{f}. According to Fig. 3, the vectors can be decomposed into

$$\begin{cases} e\cos\theta_e^{\mathrm{P}} = v\cos\theta_v^{\mathrm{P}} - X_{\mathrm{f}}i_q \\ e\sin\theta_e^{\mathrm{P}} = v\sin\theta_v^{\mathrm{P}} + X_{\mathrm{f}}i_d \end{cases}. \tag{19}$$

The linearization of (19) is

$$\begin{cases} \cos\theta_{e0}^{\mathrm{P}}\Delta e - e_0\sin\theta_{e0}^{\mathrm{P}}\Delta\theta_e^{\mathrm{P}} \\ \quad = \cos\theta_{v0}^{\mathrm{P}}\Delta v - v_0\sin\theta_{v0}^{\mathrm{P}}\Delta\theta_v^{\mathrm{P}} - X_{\mathrm{f}}\Delta i_q \\ \sin\theta_{e0}^{\mathrm{P}}\Delta e + e_0\cos\theta_{e0}^{\mathrm{P}}\Delta\theta_e^{\mathrm{P}} \\ \quad = \sin\theta_{v0}^{\mathrm{P}}\Delta v + v_0\cos\theta_{v0}^{\mathrm{P}}\Delta\theta_v^{\mathrm{P}} + X_{\mathrm{f}}\Delta i_q \end{cases}. \tag{20}$$

As shown in Fig. 3, $\theta_{v0}^{\mathrm{P}} = 0$. In addition, as the phase angle difference between the internal voltage and the terminal voltage in steady-state is generally small, it can be assumed that $\theta_{e0}^{\mathrm{P}} \approx \theta_{v0}^{\mathrm{P}} = 0$ [24], which yields

$$\begin{cases} \sin\theta_{e0}^{\mathrm{P}} \approx \sin\theta_{v0}^{\mathrm{P}} = 0 \\ \cos\theta_{e0}^{\mathrm{P}} \approx \cos\theta_{v0}^{\mathrm{P}} = 1 \end{cases}. \tag{21}$$

Based on (21), (20) becomes

$$\begin{cases} \Delta e = \Delta v - X_{\mathrm{f}}\Delta i_q \\ \Delta\theta_e^{\mathrm{P}} = \dfrac{v_0}{e_0}\Delta\theta_v^{\mathrm{P}} + \dfrac{X_{\mathrm{f}}}{e_0}\Delta i_d \end{cases}. \tag{22}$$

The power flow characteristic of the filter should be obtained as well. When ignoring the resistance, the power flowing from the internal voltage to the terminal voltage is given as

$$\begin{cases} P = \dfrac{ev\sin(\theta - \theta_v)}{X_{\mathrm{f}}} \\ Q = \dfrac{e^2 - ev\cos(\theta - \theta_v)}{X_{\mathrm{f}}} \end{cases}, \tag{23}$$

where Q is the output reactive power from the converter. Linearizing (23) results in

$$\begin{cases} \Delta\theta = \Delta\theta_v + \dfrac{X_{\mathrm{f}}}{e_0 v_0}\Delta P \\ \Delta e = \dfrac{e_0}{2e_0 - v_0}\Delta v + \dfrac{X_{\mathrm{f}}}{2e_0 - v_0}\Delta Q \end{cases}. \tag{24}$$

According to (22) and (24), the dynamic of the filter inductor can be synthesized by

$$\begin{cases} \begin{bmatrix} \Delta\theta_v^{\mathrm{P}} \\ \Delta i_d \end{bmatrix} = \boldsymbol{M}_{\mathrm{filP}} \begin{bmatrix} \Delta\theta_e^{\mathrm{P}} \\ \Delta P \end{bmatrix} \\ \begin{bmatrix} \Delta v \\ \Delta i_q \end{bmatrix} = \boldsymbol{M}_{\mathrm{filQ}} \begin{bmatrix} \Delta e \\ \Delta Q \end{bmatrix} \end{cases}, \tag{25}$$

with $\boldsymbol{M}_{\mathrm{filP}}$ and $\boldsymbol{M}_{\mathrm{filQ}}$ being expressed as

$$\boldsymbol{M}_{\mathrm{filP}} = \begin{bmatrix} 1 & -\dfrac{X_{\mathrm{f}}}{e_0 v_0} \\ \dfrac{e_0 - v_0}{X_{\mathrm{f}}} & \dfrac{1}{e_0} \end{bmatrix}, \boldsymbol{M}_{\mathrm{filQ}} = \begin{bmatrix} \dfrac{2e_0 - v_0}{e_0} & -\dfrac{X_{\mathrm{f}}}{e_0} \\ \dfrac{e_0 - v_0}{e_0 X_{\mathrm{f}}} & -\dfrac{1}{e_0} \end{bmatrix}.$$

E. Current Controller and Faster Loops

The current reference is generated by the DC-link voltage controller, and it will then generate the reference of the internal voltage to the PWM. However, as the dynamics at the CCT or faster timescales (e.g., the PWM) are not the focus of this paper, the detailed models of them are not presented.

Accordingly, by assembling the models of all the above-presented parts, the PIV model of a grid-connected converter can be obtained, as it is shown in Fig. 4. Notably, the proposed model is an open-loop model that only reflects the characteristic of the power converter.
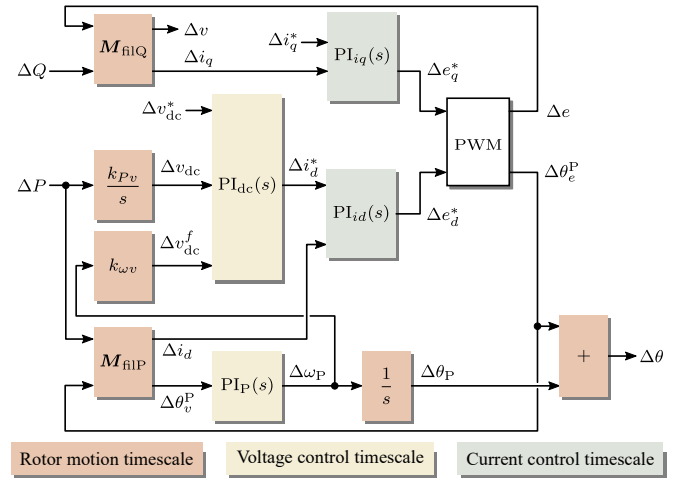
Fig. 4. Multi-timescale PIV model of grid-connected converters with the DC-link voltage control and frequency control, where PI stands for a proportional integral controller with the subscript (i.e., "dc", "P", "id", and "iq") implying the corresponding control variable.

IV. MAXIMUM VIRTUAL INERTIA IDENTIFICATION

According to Fig. 4, the PIV model of power converters basically distributes at three timescales, i.e., the RMT, the VCT, and the CCT. As the focus of this paper is on the VCT and the RMT, the submodels at these timescales should be obtained. Then, the maximum effective virtual inertia from the DC-link capacitor for a pre-designed converter (with certain control parameters, capacitor size, power level, etc.) can be identified by following the two steps:

1) Designing the maximum droop coefficient through the stability analysis at the VCT: First, the submodel at the VCT is required, where the modules at faster timescales should be ignored. Specifically, the current controllers are ignored by assuming that they can track the references immediately, i.e.,

$$\begin{cases} i_d = i_d^* \\ i_q = i_q^* \end{cases}. \tag{26}$$

By doing so, the reactive power control loop and the PWM can be neglected as well.

Consequently, one input and one output of the module $\boldsymbol{M}_{\mathrm{filP}}$, i.e., Δi_d and $\Delta\theta_e^P$, have been changed, as the current controller and the PWM module are removed. That is, the PIV model at the VCT, is obtained as shown in Fig. 5. It can be seen from Fig. 5 that the frequency regulation command from the PLL ($\Delta\omega_{\mathrm{P}}$) flows through the frequency-voltage droop controller, the DC-link voltage controller, and the filter inductor, which in turn affects the frequency tracked by the PLL. That is, the frequency-voltage droop controller couples with other controllers at this timescale, which indicates that the system stability is significantly affected by the droop coefficient $k_{\omega v}$. Thus, by analyzing the system stability at the VCT based on the model shown in Fig. 5, proper $k_{\omega v}$ can be determined. It can maintain the system stability at the VCT while providing virtual inertia as much as possible. Notably, to analyze the system stability, the PIV model of the converter should be connected to the grid model, forming the closed-loop system.
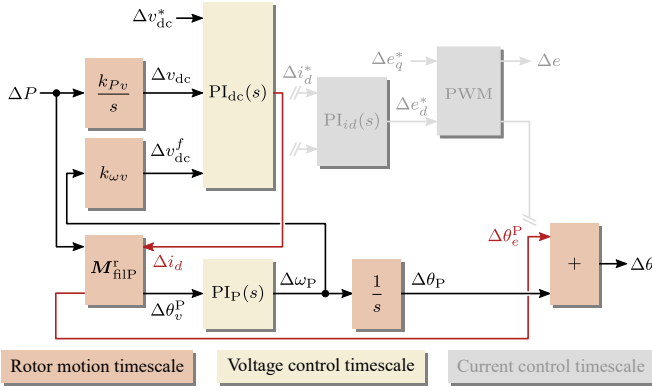
Fig. 5. PIV model simplified from Fig. 4 at the VCT, where the superscript "r" implies changes of the inputs and outputs in the corresponding module.
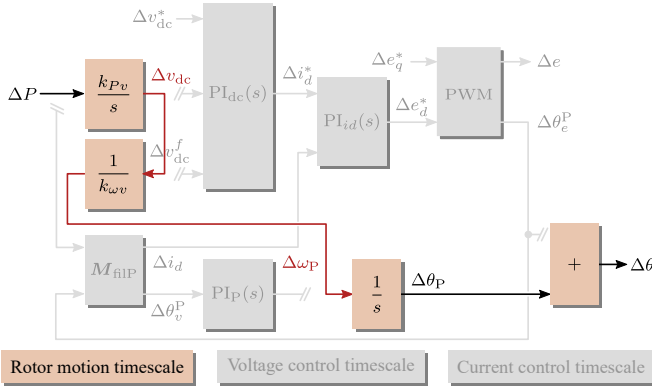

Fig. 6. PIV model simplified from Fig. 4 at the RMT.

2) Identifying the maximum effective virtual inertia based on the submodel at the RMT: After the optimal $k_{\omega v}$ is obtained, the maximum effective virtual inertia should be identified at the RMT, as the physical inertia is used to regulate the grid frequency at this timescale. The PIV model in Fig. 5 can be further simplified to the RMT, as shown in Fig. 6. When the DC-link voltage reference is considered to be constant ($\Delta v_{dc}^* = 0$), two more modules can be discarded:

- The DC-link voltage controller. It is tenable by assuming that the DC-link voltage controller can track the reference immediately, i.e., $\Delta v_{dc} = \Delta v_{dc}^f$;
- The PLL. By assuming that the PLL can track the terminal voltage phase angle immediately, the PLL can be ignored, i.e., $\Delta \theta_v^P = 0$.

It can be seen in Fig. 6 that the input and the output of $k_{\omega v}$ have changed, since the DC-link voltage controller and the PLL are removed. Notably, M_{filP} at the RMT is disabled due to two outputs being invalid. The virtual swing equation, i.e., the PIV characteristic of the converter at the RMT can be obtained from Fig. 6 as

$$\begin{cases} \Delta P = \dfrac{k_{\omega v}}{k_{Pv}} \cdot \dfrac{d\Delta \omega_P}{dt} \\ \dfrac{d\Delta \theta}{dt} = \Delta \omega_P \end{cases}, \qquad (27)$$

where ω_P can be considered to be the grid frequency due to the ignorance of the PLL at the RMT.
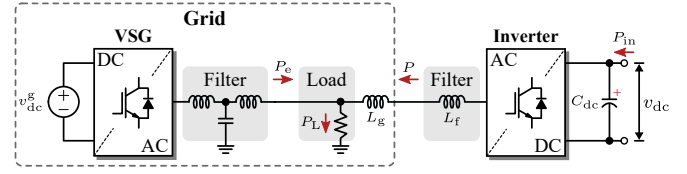
Fig. 7. Diagram of the case study system, where P_L is the load active power.

TABLE II
PARAMETERS OF THE SYSTEM IN FIG. 7.

Parameter	Description	Value
VSG		
P_{rated}^g	Rated power	2 kW
v_{rated}^g	Rated line-to-line grid voltage	0.4 kV
v_{dc}^g	Rated DC-link voltage	0.8 kV
R	Speed regulation gain	0.05 p.u.
T_G	Governor time constant	0.2 s
T_T	Turbine time constant	0.3 s
H	Inertia constant	5 s
D	Damping coefficient	1 p.u.
f^*	Rated frequency	50 Hz
L_f^{inv}	Converter-side filter inductance	4.8 mH
L_f^g	Grid-side filter inductance	2 mH
C_f^g	Filter capacitance	10 μF
L_g	Grid inductance	2 mH
Inverter		
P_{rated}	Rated power	2 kW
P_{in}	Power from DC source	0 p.u.
v_{dc}^*	DC-link voltage reference	0.8 kV
L_f	Filter inductance	5 mH
C_{dc}	DC-link capacitance	2.8 mF
(k_{p_dc}, k_{i_dc})	PI coefficients for the voltage controller	(0.5, 20)
(k_{p_P}, k_{i_P})	PI coefficients for the PLL	(0.5, 5)

It can be observed that (27) is in accordance with (6). In this case, the effective virtual inertia identified at the RMT is still represented by (7), which, however, has been properly designed with consideration of the system stability at the VCT. The quantified inertia, i.e., (7), clearly indicates the frequency support capability of the grid-connected power converters, which can be a design constraint in PEDSs.

V. MODEL VALIDATION AND CASE STUDY

In order to validate the proposed model and the maximum virtual inertia identification method, a case study is presented in this section. The overall system structure is shown in Fig. 7, which contains a VSG and a grid-feeding inverter. The VSG is applied in the case-study system to represent the AC grid and govern the grid frequency. The control system of the VSG is shown in Fig. 1, with the parameters being given in Table II.

A. Validation of the PIV Model at the VCT

The proposed model is validated first. To do so, the inverter is connected to an infinite-bus to avoid the effect of the VSG. The inverter-infinite-bus system is simulated in MAT-LAB/Simulink to validate the proposed model at the VCT, as shown in Fig. 5. At $t = 2$ s, the DC-link voltage reference increases by 5% (0.04 kV). The system responses with $k_{\omega v} = 1$
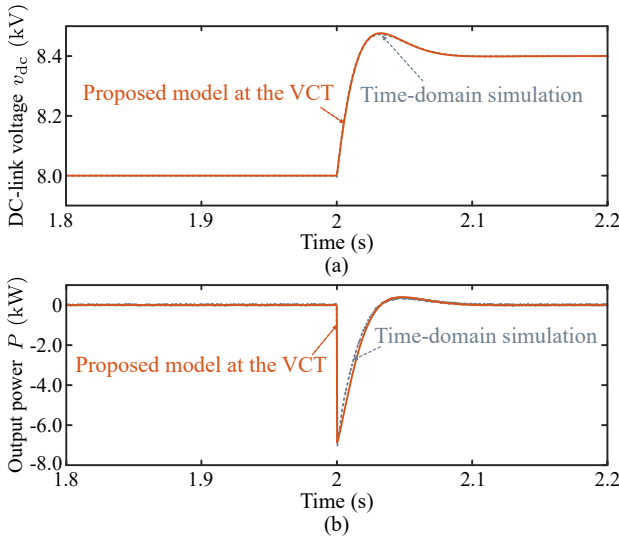
Fig. 8. Responses of the PIV model at the VCT and the time-domain simulation results when the DC-link voltage reference increases by 5%: (a) DC-link voltage and (b) inverter output power.

are shown in Fig. 8, where the dynamics of the DC-link voltage and the active power are presented. It can be seen from Fig. 8 that the responses of the systems are matching well, including the overshoots and the response dynamics. The simulation results show that the proposed PIV model for power converters at the VCT is accurate. Thus, it can be adopted for stability analysis and effective virtual inertia identification of power converters.

B. Stability Analysis and Virtual Inertia Identification

As illustrated, the design of $k_{\omega v}$, which determines the virtual inertia, should consider the system stability. To analyze the stability, the closed-loop system should be obtained, i.e., the converter model should be connected to the grid model. For practical systems, the grid parameters can be obtained from the system operator [33], whereas in this paper, the grid is represented by a VSG, as shown in Fig. 7. In such a case, focusing on the active power (related to the frequency) characteristic, the closed-loop system can be obtained. Specifically, the PIV characteristic of the closed-loop system is given as

$$\begin{cases} P_{\mathrm{e}} + P = P_{\mathrm{L}} \\ P = \dfrac{e v_{\mathrm{g}}}{X_{\mathrm{f}} + X_{\mathrm{g}}} \sin(\theta - \theta_{\mathrm{g}}) \end{cases}, \qquad (28)$$

where v_{g} is the terminal voltage of the VSG and X_{g} is the corresponding reactance for the grid inductor L_{g}. Ignoring the voltage amplitude variation, the linearized model of the grid is obtained as

$$\begin{bmatrix} \Delta P \\ \Delta P_{\mathrm{e}} \end{bmatrix} = \begin{bmatrix} 0 \\ 1 \end{bmatrix} \Delta P_{\mathrm{L}} + \begin{bmatrix} \dfrac{e_0 v_{\mathrm{g}0}}{X_{\mathrm{f}} + X_{\mathrm{g}}} & -\dfrac{e_0 v_{\mathrm{g}0}}{X_{\mathrm{f}} + X_{\mathrm{g}}} \\ -\dfrac{e_0 v_{\mathrm{g}0}}{X_{\mathrm{f}} + X_{\mathrm{g}}} & \dfrac{e_0 v_{\mathrm{g}0}}{X_{\mathrm{f}} + X_{\mathrm{g}}} \end{bmatrix} \begin{bmatrix} \Delta \theta \\ \Delta \theta_{\mathrm{g}} \end{bmatrix}. \qquad (29)$$

Combining (29) with the inverter PIV model, the closed-loop model of the system can be obtained, as it is shown in Fig. 9, based on which the stability analysis can be conducted.
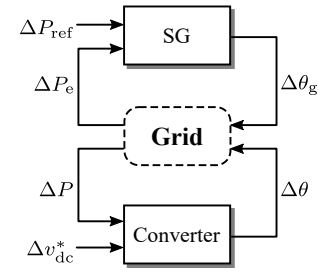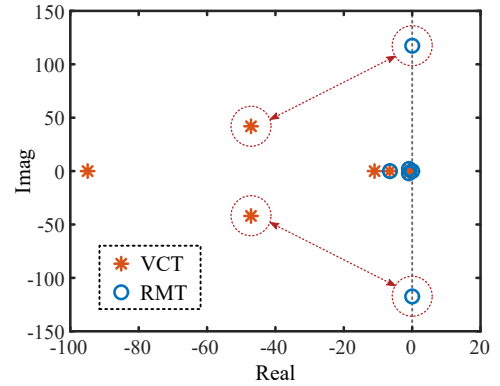

Fig. 9. Closed-loop grid-interactive system.

Fig. 10. Eigenvalues of the closed-loop systems at the VCT and the RMT when $k_{\omega v} = 1$.

As aforementioned, for a pre-design system, the maximum virtual inertia that the DC-link capacitor can provide is determined by the frequency-voltage droop coefficient $k_{\omega v}$. Thus, the impact of $k_{\omega v}$ on the system stability should be investigated. Firstly, the eigenvalues of the closed-loop systems (i.e., in Fig. 9) at the VCT and the RMT with $k_{\omega v} = 1$ are given in Fig. 10. It can be seen from Fig. 10 that the closed-loop system eigenvalues of the systems at the VCT and the RMT around the origin overlap with others, which means that the systems behave similarly at the corresponding faster timescale. However, there are a pair of eigenvalues that behave differently, as surrounded by the dashed circles in Fig. 10. In the model at the VCT, the pair of eigenvalues are at 42 rad/s, indicating that the natural frequency of these eigenvalues is within the VCT. According to the participation factor analysis, state variables Δv_{dc} and $\Delta \varphi_{\mathrm{dc}}$ participate the most in the oscillation mode corresponding to these eigenvalues. Thus, these eigenvalues may reflect the impact of the DC-link voltage controller on the closed-loop system stability. If $k_{\omega v}$ is designed based on the model at the RMT, the dynamic of the DC-link voltage controller will not be considered. Thus, $k_{\omega v}$ should be designed based on the model at the VCT.

Furthermore, the eigenvalues of the closed-loop system at the VCT with an increase of $k_{\omega v}$ from 0 to 8 are presented in Fig. 11. It can be seen from Fig. 11 that when $k_{\omega v}$ increases, the conjugated eigenvalues corresponding to the DC-link voltage controller are moving toward the right half-plane. When $k_{\omega v}$ increases from 5.5 to 6, the conjugated eigenvalues move across the imaginary axis, meaning that the system becomes unstable. Thus, $k_{\omega v}$ should not exceed 5.5 to ensure the system stability, limiting the inertia emulation.
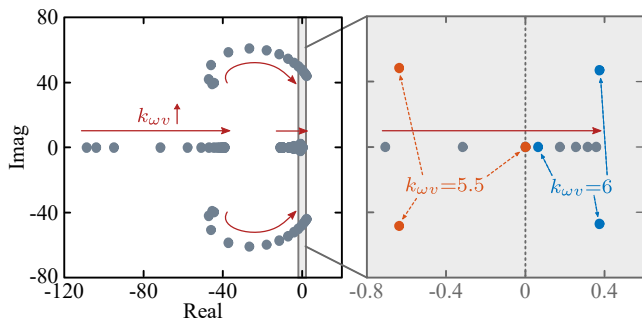
Fig. 11. Closed-loop system eigenvalues when $k_{\omega v}$ increases from 0 to 8.
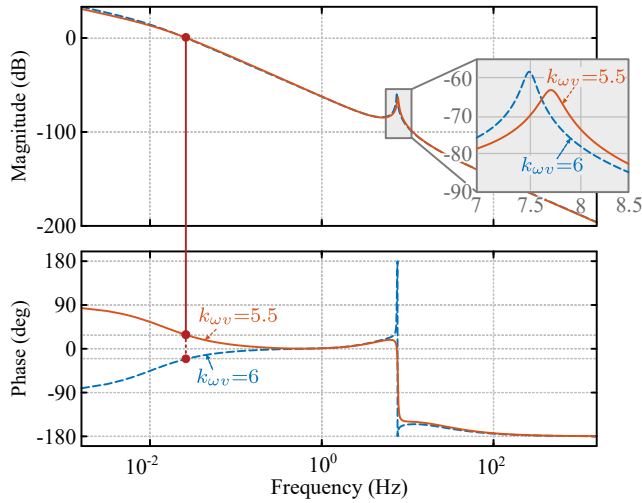

Fig. 12. Bode diagrams of the closed-loop system when $k_{\omega v}$ = 5.5 and 6.

Notably, if the closed-loop system at the RMT is applied for the eigenvalue analysis, the trajectory of the conjugated eigenvalues will not be observed, and in turn, an appropriate design of $k_{\omega v}$ cannot be ensured.

In addition, the Bode diagrams of the closed-loop system when $k_{\omega v}$ = 5.5 and 6 are obtained, as shown in Fig. 12. It can be observed in Fig. 12 that there is a resonant peak around 7.5 $\sim$ 8 Hz in both cases. When $k_{\omega v}$ = 5.5, the phase is positive, and the system is stable. However, if $k_{\omega v}$ = 6, the phase becomes negative, indicating an unstable system. The Bode diagrams further validate the eigenvalue analysis, i.e., $k_{\omega v}$ should not exceed 5.5; otherwise, the system will become unstable. Accordingly, the maximum virtual inertia can be calculated by (7) as 2.47 s. It is worth mentioning that the identified maximum effective inertia is meaningful for PEDSs in the operation and planning phases (to achieve optimal virtual inertia management).

C. Experimental Verification

The proposed virtual inertia design method is validated on a real-time hardware-in-the-loop (RT-HIL) system consisting of a controller (dSPACE/MicroLabBox) and an RT simulator (Plexim/RT-Box). Referring to Fig. 7, experimental tests are then performed with the same system parameters shown in Table II. In steady-state, the active power load is 4 kW. When
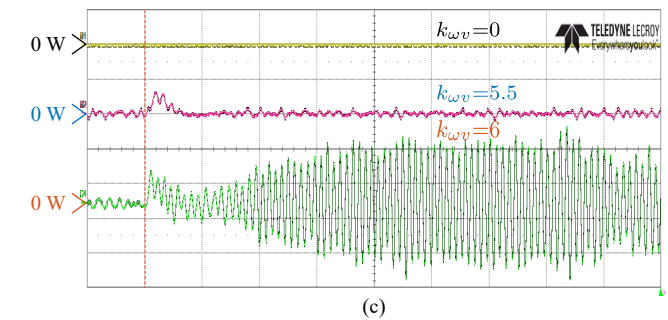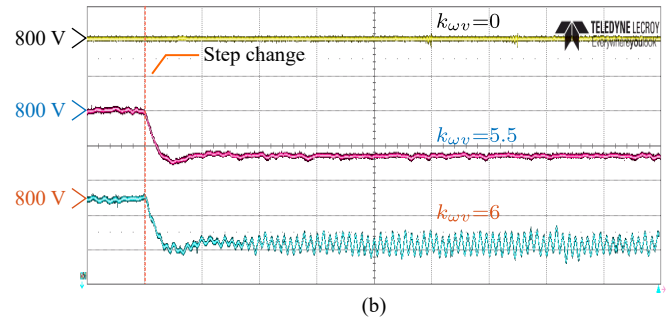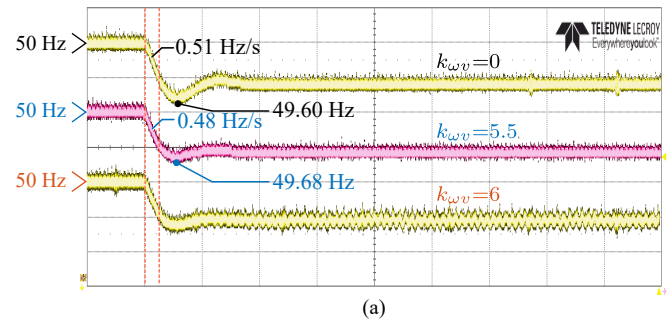

Fig. 13. Experimental results of the system under a 10%-load step when $k_{\omega v}$ = 0, 5.5 and 6: (a) grid frequency [0.25 Hz/div], (b) inverter DC-link voltage [20 V/div], and (c) inverter output power [200 W/div], time [5 s/div].
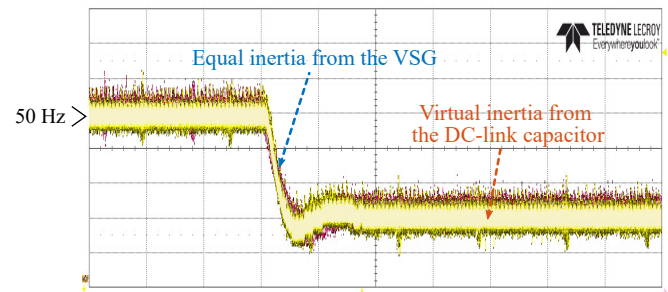

Fig. 14. Experimental results when the (virtual) inertia is from the DC-link capacitor and the VSG (time [2 s/div], frequency [0.1 Hz/div]).

t = 6 s, a 5%-load (0.1 kW) step is activated in the system under study.

The system under a 10%-load (0.2 kW) step when $k_{\omega v}$ = 0, 5.5 and 6 are tested and the results are shown in Fig. 13. It can be seen in Fig. 13 that when $k_{\omega v}$ = 0, the frequency nadir is 49.60 Hz, and the RoCoF in the first 500 ms is 0.51 Hz/s. When $k_{\omega v}$ = 5.5, the frequency-voltage droop controller is activated, which makes the DC-link capacitor to discharge active power to stabilize the grid frequency. In such a case, the frequency nadir becomes 49.68 Hz, and the RoCoF is

reduced to 0.48 Hz/s. The results demonstrate that the DC-link capacitor participates in the frequency regulation and the inertia provision. If more inertia is required, the coefficient should be increased. However, when $k_{\omega v} = 6$, the system oscillates after the load step, indicating instability. The RT-HIL experimental results validate the stability analysis and the model, where 5.5 is the maximum $k_{\omega v}$ for this pre-designed system. Notably, the method in [20] would give $k_{\omega v} = 25$ with the maximum voltage deviation being 80 V and allowed frequency deviation being 0.2 Hz. Such a design may eventually introduce instability in a long-term run.

After obtaining $k_{\omega v}$, the effective virtual inertia should be identified at the RMT for the system-level inertia improvement. With the maximum $k_{\omega v} = 5.5$, the maximum virtual inertia is calculated according to (7) as 2.47 s. To verify the virtual inertia, the system with 2.47 s virtual inertia from the DC-link capacitor is compared to the system where the equal inertia (i.e., 2.47 s) is provided by the VSG. The real-time test results with the 10%-load step are shown in Fig. 14. It can be observed from Fig. 14 that the responses of the grid-connected system with the two inertia provision schemes agree with each other, which verifies the effectiveness of the proposed model and the maximum inertia identification. This can be a useful criterion in the design phase of grid-connected converter systems in order to ensure grid stability and robustness.

Notably, although the case study was performed on a two-converter system, it is, in general, valid that the proposed multi-timescale PIV model not only balances the requirements for precision and simplicity, but also bridges well the characteristics of the power converters and SGs, and further the large-scale power grids. Based on the model, the inertia characteristics of power converters can be obtained efficiently. For a pre-designed converter, the maximum virtual inertia that the DC-link capacitor can provide with taking system stability into account can be identified. In turn, for a converter to be designed, the control parameters or the DC-link capacitor size can be fine-tuned according to the inertia emulation requirement from the grid. Ultimately, from the perspective of the grid, it becomes possible to optimally allocate, dispatch, and manage the inertia among the entire system with many power converters, which will benefit the global inertia optimization in the PEDSs.

VI. Conclusion

The maximum virtual inertia from DC-link capacitors was analyzed in this paper, which considers the impact of inertia emulation on system stability at the VCT. The analysis is based on a multi-timescale PIV model of power converters. Compared with the conventional model focusing on single timescale, the multi-timescale model facilitates applications with different focuses, and they can be connected to each other with identical external characteristics. Specifically, based on the submodel at the VCT, the system stability with the virtual inertia control of DC-link capacitor was adequately analyzed, and the virtual inertia control parameter was properly tuned. After that, the maximum virtual inertia, i.e., the effective inertia that the DC-link capacitor can provide under the certain

operation condition, was identified based on the submodel at the RMT. Both simulation and experimental results have validated the effectiveness of the proposed model. With the properly designed virtual inertia control, the system inertia can be effectively enhanced by numerous DC-link capacitors in the system. More importantly, based on the accurately identified effective virtual inertia, the future inertia placement and optimization at the system level can be expected, leading to more flexible and stable PEDSs.

References

[1] Q. Peng, Q. Jiang, Y. Yang, T. Liu, H. Wang, and F. Blaabjerg, "On the Stability of Power Electronics-Dominated Systems: Challenges and Potential Solutions," *IEEE Trans. Ind. Appl.*, vol. 55, no. 6, pp. 7657–7670, Nov. 2019.

[2] AEMO, "Black System South Australia 28 September 2016 - Final Report," Tech. Rep., Mar. 2017.

[3] National Grid ESO, "Technical Report on the Events of 9 August 2019," Wokingham, UK, Tech. Rep., Sep. 2019.

[4] J. Fang, H. Li, Y. Tang, and F. Blaabjerg, "On the Inertia of Future More-Electronics Power Systems," *IEEE J. Emerg. Sel. Top. Power Electron.*, vol. 7, no. 4, pp. 2130–2146, Dec. 2019.

[5] Hydro-Quebéc, "Technical Requirements for the Connection of Generating Stations to the Hydro-Québec Transmission System," Montréal, QC, Canada, Tech. Rep. Decision D-2018-145, Jan. 2019.

[6] IEEE Std 1547-2018 Revis. IEEE Std 1547-2003, *IEEE Standard for Interconnection and Interoperability of Distributed Energy Resources with Associated Electric Power Systems Interfaces*. New York, NY, USA: IEEE, Apr. 2018.

[7] National Grid ESO, "Frequency Response Services - Dynamic Containment," https://www.nationalgrideso.com, Apr. 2020.

[8] M. Dreidy, H. Mokhlis, and S. Mekhilef, "Inertia Response and Frequency Control Techniques for Renewable Energy Sources: A Review," *Renewable and Sustainable Energy Reviews*, vol. 69, pp. 144–155, Mar. 2017.

[9] Q. Peng, A. Sangwongwanich, Y. Yang, and F. Blaabjerg, "Grid-Friendly Power Control for Smart Photovoltaic Systems," *Solar Energy*, vol. 210, pp. 115–127, Nov. 2020.

[10] M. F. M. Arani and E. F. El-Saadany, "Implementing Virtual Inertia in DFIG-Based Wind Power Generation," *IEEE Trans. Power Syst.*, vol. 28, no. 2, pp. 1373–1384, May 2013.

[11] J. Fang, R. Zhang, H. Li, and Y. Tang, "Frequency Derivative-Based Inertia Enhancement by Grid-Connected Power Converters With a Frequency-Locked-Loop," *IEEE Trans. Smart Grid*, vol. 10, no. 5, pp. 4918–4927, Sep. 2019.

[12] A. Tayyebi, D. Groß, A. Anta, F. Kupzog, and F. Dörfler, "Interactions of Grid-Forming Power Converters and Synchronous Machines," *ArXiv190210750 Math*, Oct. 2019.

[13] B. K. Poolla, D. Groß, and F. Dörfler, "Placement and Implementation of Grid-Forming and Grid-Following Virtual Inertia and Fast Frequency Response," *IEEE Trans. Power Syst.*, vol. 34, no. 4, pp. 3035–3046, Jul. 2019.

[14] X. Meng, J. Liu, and Z. Liu, "A Generalized Droop Control for Grid-Supporting Inverter Based on Comparison Between Traditional Droop Control and Virtual Synchronous Generator Control," *IEEE Trans. Power Electron.*, vol. 34, no. 6, pp. 5416–5438, Jun. 2019.

[15] J. Driesen and K. Visscher, "Virtual Synchronous Generators," in *Proc. IEEE Power Energy Soc. (PES) Gen. Meeting*, Pittsburgh, PA, USA, Jul. 2008, pp. 1–3.

[16] U. Markovic, Z. Chu, P. Aristidou, and G. Hug, "LQR-Based Adaptive Virtual Synchronous Machine for Power Systems With High Inverter Penetration," *IEEE Trans. Sustain. Energy*, vol. 10, no. 3, pp. 1501–1512, Jul. 2019.

[17] M. Ashabani and Y. A.-R. I. Mohamed, "Novel Comprehensive Control Framework for Incorporating VSCs to Smart Power Grids Using Bidirectional Synchronous-VSC," *IEEE Trans. Power Syst.*, vol. 29, no. 2, pp. 943–957, Mar. 2014.

[18] S. A. Khajehoddin, M. Karimi-Ghartemani, and M. Ebrahimi, "Grid-Supporting Inverters With Improved Dynamics," *IEEE Trans. Ind. Electron.*, vol. 66, no. 5, pp. 3655–3667, May 2019.

[19] J. Zhu, C. D. Booth, G. P. Adam, A. J. Roscoe, and C. G. Bright, "Inertia Emulation Control Strategy for VSC-HVDC Transmission Systems," *IEEE Trans. Power Syst.*, vol. 28, no. 2, pp. 1277–1287, May 2013.

[20] J. Fang, H. Li, Y. Tang, and F. Blaabjerg, "Distributed Power System Virtual Inertia Implemented by Grid-Connected Power Converters," *IEEE Trans. Power Electron.*, vol. 33, no. 10, pp. 8488–8499, Oct. 2018.

[21] X. Huang, K. Wang, G. Li, and H. Zhang, "Virtual Inertia-Based Control Strategy of Two-Stage Photovoltaic Inverters for Frequency Support in Islanded Micro-Grid," *Electronics*, vol. 7, no. 11, p. 340, Nov. 2018.

[22] J. Fang, P. Lin, H. Li, Y. Yang, and Y. Tang, "An Improved Virtual Inertia Control for Three-Phase Voltage Source Converters Connected to a Weak Grid," *IEEE Trans. Power Electron.*, vol. 34, no. 9, pp. 8660–8670, Sep. 2019.

[23] M. Zhao, X. Yuan, J. Hu, and Y. Yan, "Voltage Dynamics of Current Control Time-Scale in a VSC-Connected Weak Grid," *IEEE Trans. Power Syst.*, vol. 31, no. 4, pp. 2925–2937, Jul. 2016.

[24] H. Yuan, X. Yuan, and J. Hu, "Modeling of Grid-Connected VSCs for Power System Small-Signal Stability Analysis in DC-Link Voltage Control Timescale," *IEEE Trans. Power Syst.*, vol. 32, no. 5, pp. 3981–3991, Sep. 2017.

[25] W. Tang, J. Hu, Y. Chang, and F. Liu, "Modeling of DFIG-Based Wind Turbine for Power System Transient Response Analysis in Rotor Speed Control Timescale," *IEEE Trans. Power Syst.*, vol. 33, no. 6, pp. 6795–6805, Nov. 2018.

[26] Y. Huang, X. Yuan, J. Hu, and P. Zhou, "Modeling of VSC Connected to Weak Grid for Stability Analysis of DC-Link Voltage Control," *IEEE J. Emerg. Sel. Top. Power Electron.*, vol. 3, no. 4, pp. 1193–1204, Dec. 2015.

[27] Q. Peng, Y. Yang, and F. Blaabjerg, "State-Space Modeling of Grid-Connected Power Converters Considering Power-Internal Voltage Characteristics," in *Proc. ICPE 2019 - ECCE Asia*, Busan, Korea, May 2019, pp. 3047–3053.

[28] J. Hu, J. Zhu, and M. Wan, "Modeling and Analysis of Modular Multilevel Converter in DC Voltage Control Timescale," *IEEE Trans. Ind. Electron.*, vol. 66, no. 8, pp. 6449–6459, Aug. 2019.

[29] L. Xiong, F. Zhuo, F. Wang, X. Liu, Y. Chen, M. Zhu, and H. Yi, "Static Synchronous Generator Model: A New Perspective to Investigate Dynamic Characteristics and Stability Issues of Grid-Tied PWM Inverter," *IEEE Trans. Power Electron.*, vol. 31, no. 9, pp. 6264–6280, Sep. 2016.

[30] H. Golpîra, H. Seifi, A. R. Messina, and M. Haghifam, "Maximum Penetration Level of Micro-Grids in Large-Scale Power Systems: Frequency Stability Viewpoint," *IEEE Trans. Power Syst.*, vol. 31, no. 6, pp. 5163–5171, Nov. 2016.

[31] P. Kundur, N. J. Balu, and M. G. Lauby, *Power System Stability and Control*. New York, NY, USA: McGraw-hill, 1994.

[32] Y. Gu, N. Bottrell, and T. C. Green, "Reduced-Order Models for Representing Converters in Power System Studies," *IEEE Trans. Power Electron.*, vol. 33, no. 4, pp. 3644–3654, Apr. 2018.

[33] E. Ørum, L. Haarla, M. Kuivaniemi, M. Laasonen, A. Jerkø, I. Stenkløv, F. Wik, K. Elkington, R. Eriksson, N. Modig, and P. Schavemaker, "Future System Inertia 2," ENTSO-E, Brussels, Belgium, Tech. Rep., Oct. 2017.

Jingyang Fang (S'15-M'19) received the B.Sc. and M.Sc. degrees in electrical engineering from Xi'an Jiaotong University, Xi'an, China, in 2013 and 2015, respectively, and the Ph.D. degree from School of Electrical and Electronic Engineering, Nanyang Technological University, Singapore, in 2019.

From May 2018 to August 2018, he was a Visiting Scholar with the Institute of Energy Technology, Aalborg University, Aalborg, Denmark. From August 2018 to August 2019, he was a Research Fellow with the School of Electrical and Electronic Engineering, Nanyang Technological University, Singapore. Since August 2019, he joined the Duke University and University of Kaiserslautern as a postdoctoral fellow. His research interests include power quality control, stability analysis and improvement, renewable energy integration, and digital control in more-electronics power systems.

Dr. Fang is the recipient of the Best Paper Award of IEEE Asia Conference on Energy, Power and Transportation Electrification (ACEPT) in 2017 and the Best presenter of IEEE International Power Electronics and Application Conference and Exposition (PEAC) in 2018. He received the Chinese Government Award for Outstanding Self-Financed Students Abroad in 2018 and the Best Thesis Award from NTU in 2019.

Yongheng Yang (SM'17) received the B.Eng. degree from Northwestern Polytechnical University, China, in 2009 and the Ph.D. degree from Aalborg University, Denmark, in 2014. He was a postgraduate student with Southeast University, China, from 2009 to 2011. In 2013, he spent three months as a Visiting Scholar at Texas A&M University, USA. Since 2014, he has been with the Department of Energy Technology, Aalborg University, where he became a tenured Associate Professor in 2018. In January 2021, he joined Zhejiang University, China, where he is now a Professor (tenure-track) at the Department of Electrical Engineering.

Dr. Yang was the Chair of the IEEE Denmark Section (2019-2020). He is an Associate Editor for several IEEE Transactions/Journals. He is a Deputy Editor of the *IET Renewable Power Generation* for Solar Photovoltaic Systems. He was the recipient of the 2018 *IET Renewable Power Generation* Premium Award and was an Outstanding Reviewer for the IEEE TRANSACTIONS ON POWER ELECTRONICS in 2018. In addition, he has received two IEEE Best Paper Awards. His current research includes the grid-integration of photovoltaic systems and multi-energy vectors with an emphasis on the power converter design, control, and reliability.

Tianqi Liu (SM'16) received the B.S. and the M.S. degrees from Sichuan University, Chengdu, China, in 1982 and 1986, respectively, and the Ph.D. degree from Chongqing University, Chongqing, China, in 1996, all in Electrical Engineering.

Currently, she is a professor in the College of Electrical Engineering, Sichuan University, Chengdu, China. Her main research interests are power system analysis and stability control, HVDC, optimal operation, dynamic security analysis and load forecast.

Qiao Peng (S'18-M'21) received the B.Eng. degree in electrical engineering from Sichuan University, Chengdu, China, in 2015 and the Ph.D. degree from Aalborg University, Denmark, in 2021.

She is currently an Assistant Research Fellow at the College of Electrical Engineering, Sichuan University, Chengdu, China. Her research interests include stability and control of power electronics-based power systems and grid-integration of renewable energy sources, especially photovoltaic systems.

Frede Blaabjerg (S'86-M'88-SM'97-F'03) was with ABB-Scandia, Randers, Denmark, from 1987 to 1988. From 1988 to 1992, he got the PhD degree in Electrical Engineering at Aalborg University in 1995. He became an Assistant Professor in 1992, an Associate Professor in 1996, and a Full Professor of power electronics and drives in 1998. From 2017 he became a Villum Investigator. He is honoris causa at University Politehnica Timisoara (UPT), Romania and Tallinn Technical University (TTU) in Estonia.

His current research interests include power electronics and its applications such as in wind turbines, PV systems, reliability, harmonics and adjustable speed drives. He has published more than 600 journal papers in the fields of power electronics and its applications. He is the co-author of four monographs and editor of ten books in power electronics and its applications.

He has received 31 IEEE Prize Paper Awards, the IEEE PELS Distinguished Service Award in 2009, the EPE-PEMC Council Award in 2010, the IEEE William E. Newell Power Electronics Award 2014, the Villum Kann Rasmussen Research Award 2014 and the Global Energy Prize in 2019. He was the Editor-in-Chief of the IEEE TRANSACTIONS ON POWER ELECTRONICS from 2006 to 2012. He has been Distinguished Lecturer for the IEEE Power Electronics Society from 2005 to 2007 and for the IEEE Industry Applications Society from 2010 to 2011 as well as 2017 to 2018. In 2019-2020 he serves a President of IEEE Power Electronics Society. He is Vice-President of the Danish Academy of Technical Sciences too.